Research Article | **Open Access**

Microstructures

Jiang *et al. Microstructures* **2026**, *6*, 2026098 **DOI:**10.20517/microstructures.2026.24

Magnetic anisotropic pinning and symmetry breaking in ruthenate superlattices

Zhongyuan Jiang[1,#], Zhiwei Zhang[2,#], Kesen Zhao[3,#], Wenjie Meng[3], Yuanyuan Zhao[2], Yubin Hou[3], Zhangzhang Cui[1], Jian Zhang[1], Zheling Shan[1], Haoliang Huang[2], Qingyou Lu[1,3], Yalin Lu[1]

Keywords: Interfacial coupling, magnetic microstructures, magnetic anisotropic pinning, spin reorientation, superlattice

Citation: Jiang, Z.; Zhang, Z.; Zhao, K.; Meng, W.; Zhao, Y.; Hou, Y.; Cui, Z.; Zhang, J.; Shan, Z.; Huang, H.; Lu, Q.; Lu, Y. Magnetic anisotropic pinning and symmetry breaking in ruthenate superlattices. *Microstructures* **2026**, *6*, 2026098. https://dx.doi.org/10.20517/microstructures.2026.24

Received: 15 Feb 2026
First Decision: 16 Apr 2026
Revised: 7 May 2026
Accepted: 12 Jun 2026
Published: 2/ Jul 2026

Academic Editor: Jun Chen
Copy Editor: Shu-Yuan Duan
Production Editor: Shu-Yuan Duan

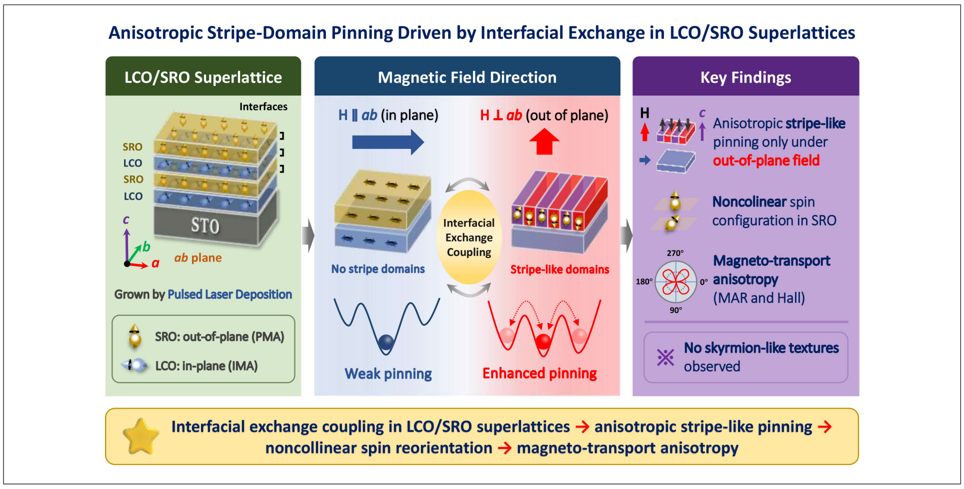

Abstract

Interfacial engineering enables various emergent effects such as spin reorientations and transport anisotropy. Noncollinear spin textures are essential for realizing many emergent quantum transport phenomena. However, driving such spin structures requires precise control of the interfacial magnetic coupling in complex oxide heterostructures. Here, by utilizing competing exchange interactions at the interface between ferromagnetic metal $SrRuO_3$ and ferromagnetic insulator $LaCoO_3$, we investigated a noncollinear spin configuration in $SrRuO_3$ sublayers. Stripe-like domains were induced by out-of-plane rather than in-plane magnetic fields, indicating strong anisotropy pinning in our superlattices. The observed magneto-transport anisotropy can be well explained by our proposed spin reorientation configurations. No magnetic skymionic textures were observed in our superlattice samples. The interfacial exchange interaction may compete with the

[1]Hefei National Laboratory, Anhui Laboratory of Advanced Photon Science and Technology, Hefei National Laboratory for Physical Sciences at the Microscale, University of Science and Technology of China, Hefei 230026, Anhui, China.
[2]Quantum Science Center of Guangdong-Hong Kong-Macao Greater Bay Area, Shenzhen 518045, Guangdong, China.
[3]Anhui Province Key Laboratory of Condensed Matter Physics at Extreme Conditions, High Magnetic Field Laboratory, Chinese Academy of Sciences, Hefei 230031, Anhui, China.
[#]These authors contributed equally to this work.

Correspondence to: Dr. Haoliang Huang, Quantum Science Center of Guangdong-Hong Kong-Macao Greater Bay Area, Shenzhen 518045, Guangdong, China. E-mail: huanghaoliang@quantumsc.cn; Pro. Qingyou Lu, Anhui Province Key Laboratory of Condensed Matter Physics at Extreme Conditions, High Magnetic Field Laboratory, Chinese Academy of Sciences, Hefei 230031, Anhui, China. E-mail: qxl@ustc.edu.cn; Prof. Yalin Lu, Hefei National Laboratory, Anhui Laboratory of Advanced Photon Science and Technology, Hefei National Laboratory for Physical Sciences at the Microscale, University of Science and Technology of China, Hefei 230026, Anhui, China. E-mail: yllu@ustc.edu.cn

Dzyaloshinskii-Moriya interaction (DMI) that stabilizes skyrmions, featuring a higher exchange coupling energy than that for the topological spin textures according to our micromagnetic simulations. Our work highlights the potential of interfacial engineering in tuning the spintronic properties by designing proper interfacial interactions.

INTRODUCTION

Interfacial engineering in complex correlated oxide heterostructures has emerged as a powerful paradigm for designing novel quantum states of matter. At atomic-layer-thick interfaces, lattice strain[1-4], electronic reconstruction[5,6], superconducting pairing[7-9] and spin reorientation[10] can give rise to various emergent phenomena not found in the constituent bulk materials. These engineered quantum phases hold significant potential for next-generation electronic and quantum information technologies. For example, customized interface exchange coupling can be achieved by delicately regulating the selection of the bulk materials, growth conditions as well as the design of the inter-layers, thereby obtaining spintronic functions designed on demand[1,4,11]. In particular, when two materials with distinct magnetic orders form an interface, the mismatch of spin configurations at the interface will induce significant magnetic proximity effects and lead to abnormal electronic transport characteristics[12-14], providing an ideal platform for exploring novel quantum phenomena.

$SrRuO_3$ (SRO), for instance, is a well-known itinerant ferromagnet (T_C ~ 120 K) with unique transport and magnetic properties. SRO-based interfaces can host multiple interesting effects, such as interfacial oxygen distortion, strain-induced anisotropy, anomalous Hall effect (AHE), and skyrmionic spin textures, offering potential routes to design switches of various spintronic behaviors[2,15-24]. In magnetic thin films and heterostructures, the competition among Heisenberg exchange, magnetic anisotropy, dipolar interaction, and long-range magnetic order commonly gives rise to spatially modulated magnetic order, including stripe-like or labyrinthine domain patterns[25,26]. Magnetic skyrmions, in contrast, represent a more specific class of topological spin textures that usually require suitable symmetry breaking, Dzyaloshinskii-Moriya interaction (DMI), magnetic anisotropy, and appropriate magnetic-field and temperature conditions[10,16,17,24]. It is worth noting that the specifically designed SRO heterostructures exhibit hump-shaped Hall resistivity arising at particular field strengths and temperatures, which is sometimes alternatively attributed to the topological Hall effect (THE) associated with magnetic skyrmions[27-29], although its origin remains highly debated[30-33]. Therefore, direct magnetic-domain imaging is important for distinguishing skyrmion-like textures from stripe-like magnetic domains.

Furthermore, SRO can exhibit perpendicular magnetic anisotropy (PMA) under compressive strain with the spin orientation preferring the film-normal direction[34-36]. In contrast, while a non-magnetic insulator ground state in bulk, tensile-strained $LaCoO_3$ (LCO) thin films can stabilize a ferromagnetic (FM) insulating phase with a lower Curie temperature (75 ~ 85 K) and exhibit in-plane magnetic anisotropy (IMA)[37]. This stark contrast, i.e., a strained FM metal with PMA (SRO) adjacent to a strained FM insulator with IMA (LCO), creates an ideal interface for generating profound magnetic frustration and symmetry breaking. The direct exchange coupling at such an interface is expected to compete with the intrinsic anisotropy of each layer, providing a possible route to noncollinear spin reorientation, exotic domain structures, and manipulation of topological defects.

In this study, high-quality LCO/SRO superlattices were prepared to investigate the interfacial spin reorientation and magnetic anisotropy in oxide heterostructures. We observe stripe-like magnetic domains with pronounced anisotropy in the LCO/SRO superlattices. No skyrmion-like circular spin textures are observed in our magnetic force microscopy (MFM) measurements within the explored temperature and magnetic-field range. Based on the MFM, angular magneto-resistance, Hall transport, and micromagnetic simulation results, we propose that noncollinear ferromagnetic spin reorientation may occur at the LCO/SRO interfaces. The observed stripe-like magnetic domains and magneto-transport anisotropy are consistent with this interpretation, providing experimental support and a useful perspective for understanding and tuning anisotropic magnetic textures in oxide superlattices with competing interfacial magnetic interactions.

MATERIALS AND METHODS

Thin film deposition and superlattice preparation

The superlattices $(LCO_M/SRO_N)_{12}$ (denoted by L_MS_N, where M and N denote the number of unit cells of LCO and SRO, respectively, in each bilayer period, and the subscript 12 indicates 12 repetitions of the LCO/SRO bilayer) were grown on TiO_2-terminated $SrTiO_3$ (STO) substrates (from MTI Corporation Inc., China) by pulsed laser deposition (PLD, PASCAL Co., Ltd. Japan) assisted with reflection high energy electron diffraction (RHEED). We have successfully designed and prepared various superlattices, among which L_9S_6, L_7S_6, and L_5S_5 were particularly investigated. During the growth of the superlattices, the substrate temperature, oxygen partial pressure, and repetition rate of the laser pulse were 750°C, 100 mTorr, and 2 Hz, respectively. The laser fluence set at ~ 2 J cm^{-2} for the SRO layer and 1.2 J cm^{-2} for the LCO layer.

X-ray characterizations and scanning transmission electron microscopy

X-ray characterizations, including X-ray diffraction (XRD), X-ray reflectivity (XRR), and reciprocal space mapping (RSM), of the superlattices were performed using a four-circle diffractometer (Cu Kα, SmartLab, Rigaku, Japan). Scanning transmission electron microscopy (STEM) was performed using an FEI Titan Themis G2 (FEI, USA), equipped with a double spherical-aberration corrector and a high brightness field-emission gun. The cross-section of the specimens was prepared using a FEI Helios 600i dual-beam FIB/SEM machine. Pt electron-beam deposition and C ion-beam deposition were conducted in order to protect the sample surface from beam damage. Both X-ray characterization and STEM experiments were conducted at room temperature.

Magnetic force microscopy

MFM measurements were performed on the top surface of the superlattice films in a 12 T superconducting magnet placed in ultrahigh vacuum at the High Magnetic Field Laboratory in Hefei, China. The spatial resolution of the microscope is 10 nm. A rotation sample plate is mounted on the axis, allowing for an *in-situ* field angle ranging from 0° to 180°. For signal detection, we utilized custom piezoresistive cantilevers (SCL-Sensor Tech., PRSA-L300-F50-STD) characterized by a hollow beam structure and a resonance frequency of ~ 37 kHz. The tips were magnetically coated with a Ti (5 nm)/Co (30 nm)/Au (5 nm) film using electron beam evaporation and pre-magnetized perpendicular to the cantilever beam. The readout electronics consisted of a home-made active Wheatstone bridge preamplifier (gain 1,000×) interfaced with a commercial RHK R9 controller. Topographic images were acquired in tapping mode, while MFM images were acquired in constant-height mode approximately 100 nm above the sample surface. The resulting MFM contrast maps the resonant frequency shift caused by the out-of-plane stray field gradient, where dark and light regions represent attractive and repulsive magnetic forces, respectively. Post-processing of the SPM data was conducted using WSxM. All MFM images presented in this work were measured on the top surface of the as-grown superlattice films. Cross-sectional MFM was not performed in this study. The superlattice terminates with an SRO layer (topmost surface). The MFM probe detects magnetic stray fields emanating from this top SRO layer. The signal primarily reflects the magnetization state of the SRO layer because: SRO is metallic and ferromagnetic with strong stray-field contrast, while LCO is insulating with weak magnetic contrast at the measurement temperatures (5-300 K), and the 6uc (~ 2.4 nm) top SRO thickness is within the typical MFM detection depth.

Magnetic-field-angle-dependent resistivity

All transport measurements were performed using a physical property measurement system (PPMS, Quantum Design, USA) equipped with a sample rotator. The magnetic-field-angle-dependent resistivity (MAR) is defined as MAR = $[\rho(\theta) - \rho(0^\circ)]/\rho(0^\circ)$, where θ is the angle of the magnetic field with respect to the film normal (e.g. 0° for field pointing out-of-plane). For the transport measurements, Hall electrodes were fabricated using the evaporation method. The current was applied in the plane of the film along the [100] direction of the STO substrate, and the magnetic field was rotated in the plane perpendicular to the current direction (the *ac* plane), with $\theta = 0°$ corresponding to the field applied perpendicular to the film plane.

Static micromagnetic simulation

An all-Python-based micromagnetic framework were employed that computes the magnetostatic field via 3D fast Fourier transform (FFT) convolution and the magnetization is relaxed toward a steady state through an energy-minimization alignment scheme. At each iteration the local moment is rotated toward the direction of the effective field with a damping-like coefficient serving purely as a convergence parameter until the system reaches a local energy minimum. The micromagnetic simulations were performed under two regimes: (A) a DMI-dominated regime and (B) an interfacial-exchange-dominated regime. The total energy functional includes exchange, uniaxial anisotropy (PMA for SRO, IMA for LCO), demagnetizing (computed via FFT-based convolution), interfacial DMI, Zeeman, and an effective interfacial exchange interaction term at the LCO/SRO boundary. The 2D model simulation and its comparison with the standard GPU-based solver mumax3 are provided in Supplementary Table 1. The parameters used for SRO and LCO layers are summarized in Supplementary Table 2, while the parameters used for Case A and Case B are listed in Supplementary Table 3.

Anomalous hall effect analysis

The Hall resistivity was analyzed using a two-channel AHE model, which is expressed as $\rho_{xy} = R_1M_1 + R_2M_2 + \rho_{xy}^{OHE}$, where R_1 and R_2 are the anomalous Hall coefficients of two distinct magnetic channels, M_1 and M_2 are their respective magnetizations, and ρ_{xy}^{OHE} is the ordinary Hall resistivity. The two channels are assigned to represent the bulk-like SRO ferromagnetic component (weakly coercive S-loop) and the interfacial ferromagnetic coupling component (highly coercive L-loop), respectively. The model parameters were determined by least-squares fitting to the experimental Hall data. We note that this phenomenological model assumes isotropic magnetic properties and does not account for possible contributions from noncollinear spin textures or inhomogeneous magnetization distributions.

RESULTS AND DISCUSSION

Atomically layer-by-layer growth

LCO/SRO superlattices were prepared by alternating growth of LCO and SRO on top of TiO_2-terminated STO substrates. Figure 1A shows the conceptual stacking of the LCO and the SRO layers on STO. The STEM image identifies each atomic layer with no ambiguity. RHEED images during sample preparation were captured for the three sets of samples [Figure 1B-D], which present the layer-by-layer nature of the growth. XRD measurements [Figure 1E] show rigid epitaxy of the superlattice to the substrate according to the result of the (002) substrate peak and the superlattice satellite peaks (SL0, ±1, ±2), including beating patterns due to the whole film thickness and the satellite peaks (SLx) due to each LCO/SRO layer pair. The XRR patterns were in good agreement with the theoretical fit for L_9S_6, L_7S_6 and L_5S_5 structures, respectively [Figure 1F]. The combination of RHEED, STEM, XRD and XRR shows the high atomic layer-by-layer quality for all of our superlattice samples.

The lattice constants of bulk STO, LCO, and SRO are approximately 3.905 Å, 3.837 Å, and 3.923 Å, respectively. Reciprocal space mapping (RSM) around the (103) reflection was performed to determine the in-plane lattice parameters of the superlattices [Supplementary Figure 1]. The RSM results confirm that the

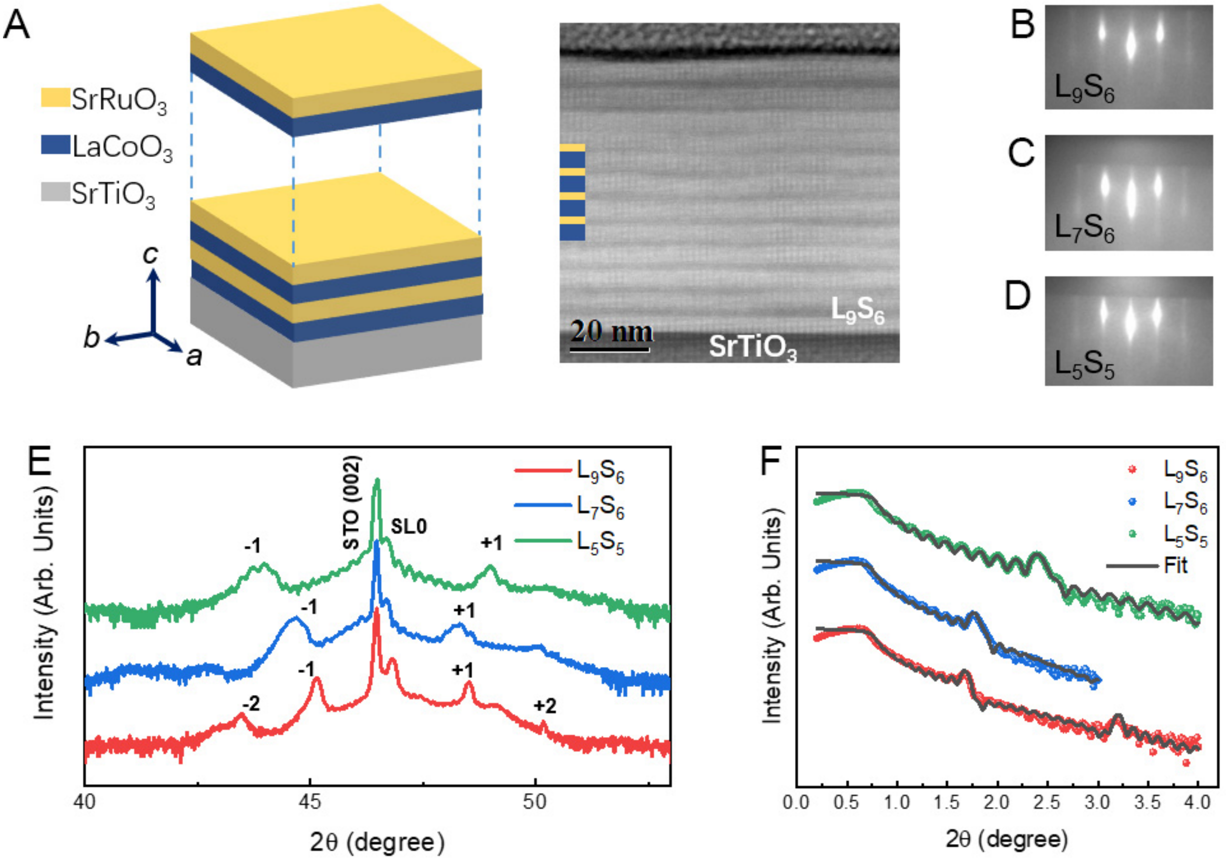

Figure 1. Structural characterization of LCO/SRO superlattices. (A) Schematic illustration of the superlattice structure (left) and cross-sectional STEM image of the L_9S_6 sample (right), showing atomically sharp interfaces between LCO (blue) and SRO (yellow) layers grown on STO substrate (gray). The scale bar represents 20 nm; (B-D) RHEED patterns along the [100] azimuth for L_9S_6, L_7S_6, and L_5S_5, respectively; (E) XRD θ-2θ scans around the (002) reflection, showing the substrate peak (STO), the superlattice zero-order peak (SL0), and satellite peaks (±1, ±2) arising from the artificial periodicity; (F) XRR data (symbols) and theoretical fits (solid lines) for the three superlattice samples. Well-defined Kiessig oscillations demonstrate an agreement between experimental data and fits for the designed layer thicknesses. LCO: $LaCoO_3$; SRO: $SrRuO_3$; STEM: scanning transmission electron microscopy; XRD: X-ray diffraction; XRR: X-ray reflectivity; STO: $SrTiO_3$.

superlattices are coherently strained to the STO substrate. The SRO and LCO suffer from compressive and tensile strain, respectively. This corresponds to a tensile strain of +1.8% for LCO and a compressive strain of -0.5% for SRO. The out-of-plane lattice parameters were determined from the XRD data, showing elongation consistent with the Poisson effect under biaxial compressive strain. The strain state is an important factor influencing the magnetic anisotropy of both LCO and SRO layers, as compressive strain in SRO is known to favor perpendicular magnetic anisotropy, while tensile strain in LCO can stabilize ferromagnetic order with in-plane magnetic anisotropy.

Magnetic anisotropic pinning

We performed the cryogenic MFM measurements to directly image the magnetic domain evolution for our superlattice samples. Here, we focus on the L_9S_6 samples. Figure 2A shows a series of the MFM images at 75 K with the field applied perpendicular to the film plane and swept in a complete loop. Stripe-like domains emerge at ~ 1 T, become saturated at higher field strengths, and reappear as the field strength decreases back to 1 T in both positive and negative field-scanning directions. Figure 2B shows corresponding MFM images at 25 K. A notable difference is that at lower temperature, stripe-like domains appear at smaller field strength (denoted from cyan brackets) and persist to higher fields, indicating enhanced magnetic anisotropy pinning.

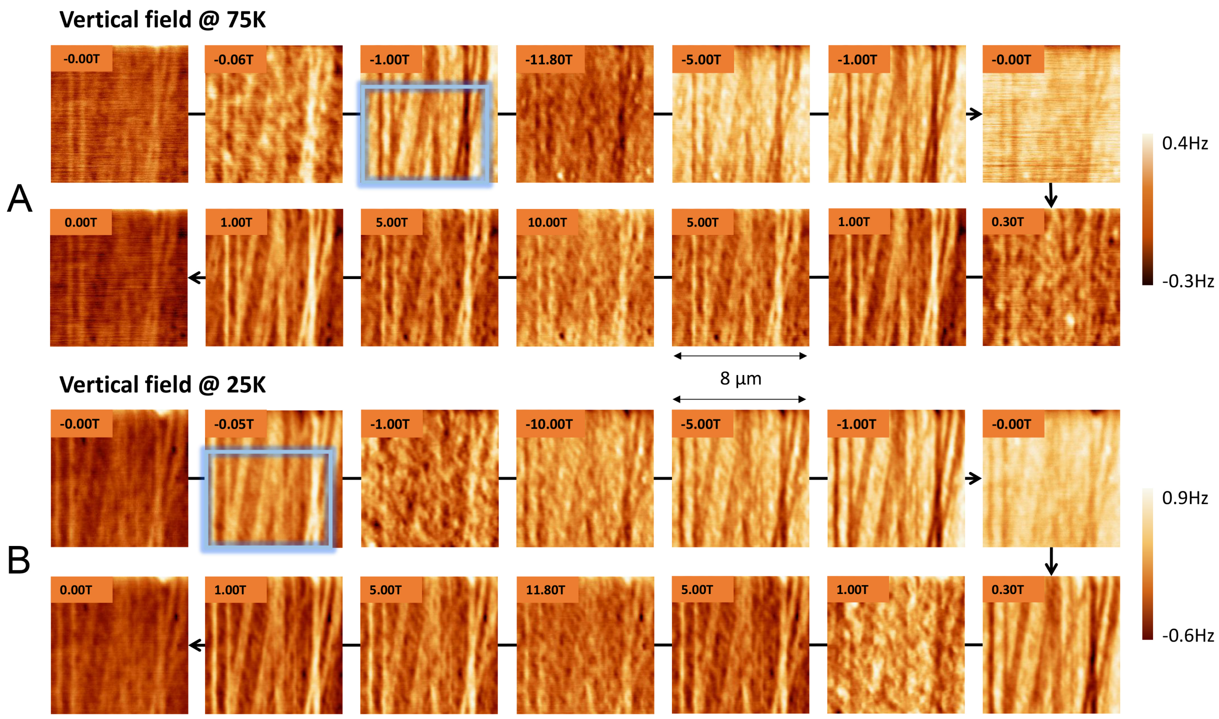

Figure 2. Magnetic-field-dependent top-surface MFM images of L_9S_6 super lattice under out-of-plane magnetic fields. (A)MFM images acquired at 75 K during a magnetic field loop applied along the out-of-plane direction. The magnetic field sequence is: -0.00 T → -0.06 T → -1.00T → -11.80 T → -5.00 T → -1.00 T → -0.00T → 0.30 T → 1.00 T → 5.00 T → 10.00 T → 5.00 T → 1.00 T → 0.00 T. The blue box high lights the field region (-1.00T) where stripe-like domains exhibit optimal contrast; (B) Corresponding MFM images at 25 K with the field sequence: -0.00 T → -0.05 T → -1.00 T → -10.00 T → -5.00 T → -1.00 T → -0.00 T → 0.30 T → 1.00 T → 5.00 T → 11.80 T → 5.00 T → 1.00 T → 0.00 T. Arrows indicate the field sweep directions. No circular skyrmion-like features are observed even at fields up to 11.8 T. The colour scales for images in A (in arrow order) are 0.18, 0.65, 0.55, 0.35, 0.55, 0.7, 0.16, 0.65, 0.55, 0.55, 0.5, 0.4, 0.65, and 0.16 Hz, respectively. The colour scales for images in B (in arrow order) are 0.2, 1.5, 0.8, 0.65, 1.0, 1.1, 0.16, 1.3, 0.8, 0.9, 0.8, 1.0, 0.9, and 0.2 Hz, respectively. MFM: Magnetic force microscopy.

Complete sets of MFM loop measurements with out-of-plane fields can be found in Supplementary Figures 2-5. The stripe-like domains are stabilized at intermediate fields (~ 1 T), but disperse at both low fields (< 0.5 T, near demagnetized state) and high fields (> 7 T, field-polarized state). By contrast, when the field is applied in-plane, no magnetic stripe is observed even at 10 T [Supplementary Figure 6 and 7], demonstrating that the stripe formation is highly anisotropic and favored by out-of-plane magnetic fields. While magnetic anisotropy has been reported in similar materials[38-40], the particular stripe morphology observed here appears to be characteristic of this superlattice architecture.

Symmetry analysis and phase diagram of MAR evolution

To further investigate the magnetic anisotropy, we conducted the MAR measurements as a function of temperature and magnetic field. MAR plots for different experimental conditions are presented in Figure 3 for the L_9S_6 samples. Forward and backward field-angle scans are shown in Supplementary Figure 8. Hysteretic behavior of magneto-resistivity, indicative of coercive ferromagnetism, is observed but diminishes as higher temperature elevates the thermal fluctuations and higher field enhances the magnetization alignment. More importantly, a purely two-fold symmetric MAR signal would be expected if the SRO magnetization maintains a single, fixed orientation. Therefore, the emergence of any higher-order symmetry component may imply intrinsic spin reorientations within the SRO layers.

To quantitatively characterize the evolution of the MAR symmetry, we developed a harmonic decomposition model to assess the magneto-transport anisotropy. The MAR signal was fitted with three components, one two-fold and one four-fold and one eight-fold, capturing the dominant symmetries: MAR(θ) = A_0 + A_2cos(2θ

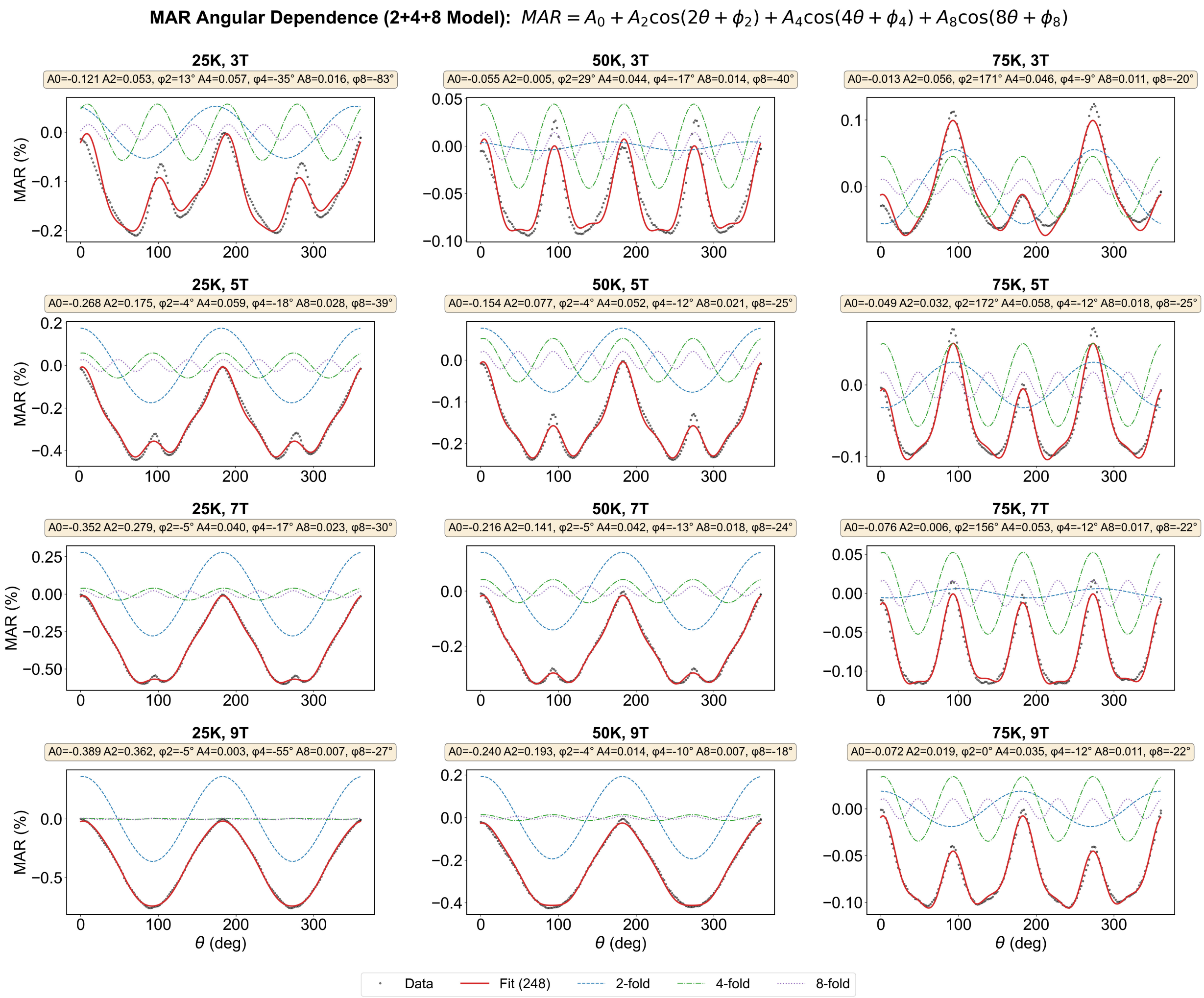

Figure 3. Harmonic decomposition of MAR results for L_9S_6, based on "2 + 4 + 8" model consisting of a two-fold, a four-fold and an eight-fold component. The original data are in grey circles. Fit curves are red solid lines. The two-fold, four-fold and eight-fold curves are blue, green and orange dashed lines, respectively. The inset brackets present the fitting results for each measurement condition. MAR: Magnetic-field-angle-dependent resistivity.

$+ \varphi_2) + A_4\cos(4\theta + \varphi_4) + A_8\cos(8\theta + \varphi_8)$, where A_2, A_4, and A_8 are the amplitudes, and φ_2, φ_4, φ_8 are the remnant phases of the two-fold, four-fold and eight-fold components, respectively. The results were plotted in Figure 3. It is noted that a two-component decomposition with one two-fold and one four-fold underfits the MAR signal though A_4/A_2 still appears to be a good order parameter for the symmetry and its evolution with field and temperature (see Supplementary Figures 9 and 10), assuring the necessity of the eight-fold component. The two-fold component originates from the uniaxial anisotropy of the SRO layer with its spin canted by interfacial exchange coupling. The four-fold component arises from the superposition of contributions from multiple SRO sublayers with different spin orientations. The eight-fold component captures higher-order angular anisotropy from crystal symmetry breaking and spin-orbit coupling, consistent with eight-fold symmetry reported in other SRO superlattice systems[41].

The fitting results reveal several important features. The systematic evolution of the three-component (2-fold, 4-fold and 8-fold) amplitudes with field and temperature is summarized in Supplementary Figure 11. The phase diagrams provide crucial quantitative support for the presence of spin reorientation. First, the amplitude A_2 of the dominant component increases monotonically with field strength at all temperatures, reflecting the progressive alignment of the bulk-like SRO spins toward the field direction. The secondary

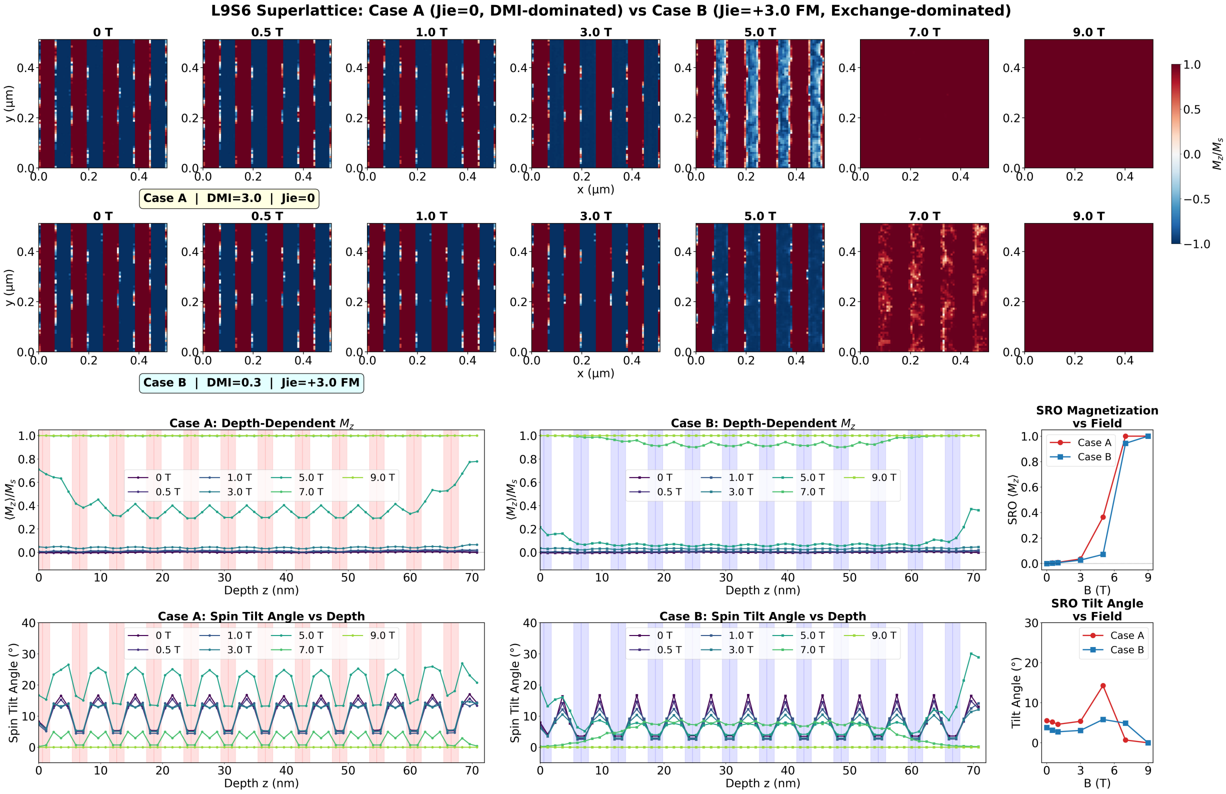

Figure 4. Micromagnetic simulation results for L_9S_6 structure under two regimes, Case A: the DMI-dominated regime and Case B: interfacial-exchange-dominated regime. The upper panel: M_z spatial distribution maps with different field strength from 0 to 9 T applied in the out-of-plane direction. The color bar denoted the magnetization ratio. The lower panel: depth-dependent magnetization profiles. Field dependence of SRO magnetization and average spin tilt angle is also provided. DMI: Dzyaloshinskii-Moriya interaction; SRO: $SrRuO_3$.

amplitudes A_4 and A_8 exhibit more complex field dependence, with non-monotonic evolution that reflects the competing effects of field-induced alignment, interfacial exchange pinning, and higher-order crystal symmetry. At 25 K, the two-fold amplitude A_2 show systematic field-dependent evolution, where the interfacial coupling is strongest. At 75 K, the 3 T and 5 T data show anomalous four-fold dominance due to proximity to the LCO Curie temperature, while the 7 T and 9 T data exhibit significantly reduced amplitudes as spins are highly aligned by strong fields.

Vertically varying noncollinear spin reorientation

To provide additional support of the competition between interfacial exchange coupling and DMI in the LCO/SRO superlattice, we performed 2D magnetostatic energy minimization simulations. Figure 4 shows the M_z spatial distribution maps and depth-dependent magnetization profiles. The simulation of the SRO magnetization at different magnetic fields is summarized in Supplementary Table 4. The magnetic stripe domains are saturated by field $\lesssim$ 7 T for the DMI-dominated regime (Case A) and field $\lesssim$ 9 T for the interfacial-exchange-dominated regime (Case B), indicating that the interfacial exchange interaction competes with the Zeeman energy. The depth-resolved magnetization profiles reveal a field-driven spin reorientation: at zero field, the average spin tilt angle $\theta \approx 5.5°$ for Case A and $\theta \approx 3.8°$ for Case B (with respect to out-of-plane direction), consistent with stripe-domain formation; with increasing field, θ increases to maximum at 5 T and decreases back to 0° at 9 T, reflecting the competition between the applied Zeeman energy and the interfacial exchange coupling. The average tilt angle of SRO spins at 5 T is ~ 15° for Case A and ~ 8° for Case B, consistent with the effect of DMI in stabilizing chiral or stripe-spiral textures. Since the thickness of each SRO layer (2.4 nm) is comparable to the exchange length, the entire layer responds coherently to interfacial coupling rather than maintaining a bulk-like out-of-plane orientation. This systematic canting favors the formation of anisotropic stripe domains.

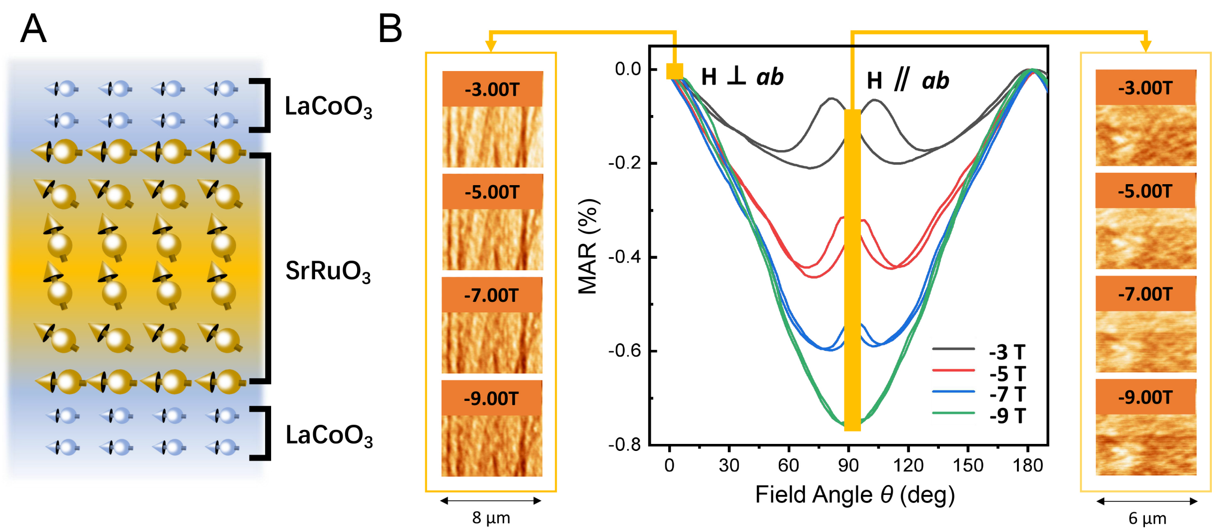

Figure 5. Field-driven evolution of spin configuration and its correlation with magnetoresistance anisotropy. (A) Schematic illustration of the proposed noncollinear spin configuration in the SRO layer. The spin orientation evolves from PMA (bulk-like, orange region) to canted (interface region, yellow) to IMA (LCO bulk, blue arrows); (B) MAR *vs.* θ at 25 K for various magnetic fields (-3 T to -9 T). Left panel: MFM images acquired at θ = 0° (H ⊥ *ab*). Right panel: MFM images acquired at θ = 90° (H ∥ *ab*). MFM: Magnetic force microscopy; IMA: in-plane magnetic anisotropy; SRO: $SrRuO_3$; PMA: perpendicular magnetic anisotropy; MAR: magnetic-field-angle-dependent resistivity.

With the MAR analysis and the simulation results, we therefore propose a vertically evolving spin texture within the SRO layers, driven by interfacial exchange coupling between the PMA-SRO and the IMA-LCO [Figure 5A]. The coupling may cant SRO spins adjacent to the interface toward the in-plane direction (inheriting the IMA of LCO), while SRO spins in the layer interior retain a stronger tendency toward the out-of-plane orientation (reflecting the PMA of bulk SRO). The phase evolution of the harmonic components directly demonstrates the proposed field-driven spin reorientation: as the magnetic field increases, the spin orientations in different SRO sublayers rotate at different rates, changing the relative phases of their transport contributions (See Supplementary Figure 12). The phase difference φ_4 - φ_2 ≈ -48° at 25 K, 3 T and -10° at 25 K, 5 T, directly demonstrating the field-driven spin reorientation.

This proposed noncollinear spin-reorientation model also suggests a correlation of the magneto-transport properties to the magnetic anisotropic stripe pinning. Figure 5B shows the MAR vs. θ plot for various fields at 25 K. The minimal resistivity occurs at θ = 90° (in-plane field), where no magnetic stripe is formed. The stripe-like domain formation introduces localized exchange interaction and enhanced scattering, thereby suppression of conductivity. Nevertheless, direct verification of the proposed vertically varying spin configuration would benefit from techniques such as polarized neutron reflectometry.

AHE and topological properties

Our MFM results found no signature of the skyrmion structure, which is nanoscale chiral magnetic spot and is often regarded as topological Hall features. The absence of skyrmion-like features in our samples might be the result of the competition between interface exchange interactions and DMI[40-44]. Figure 6 shows field-dependent Hall resistivity (after subtracting the ordinary Hall contribution) at 25 K with vertical magnetic fields, overlaid with MFM images at corresponding fields. Green symbols represent experimental data, and the red curve shows a fit using the conventional two-channel AHE model also conducted in earlier works[31,32,45]. The fitting quality is reasonable except near the peak and valley regions (~ ±1.2 T), where significant deviations occur (See Supplementary Figure 10).

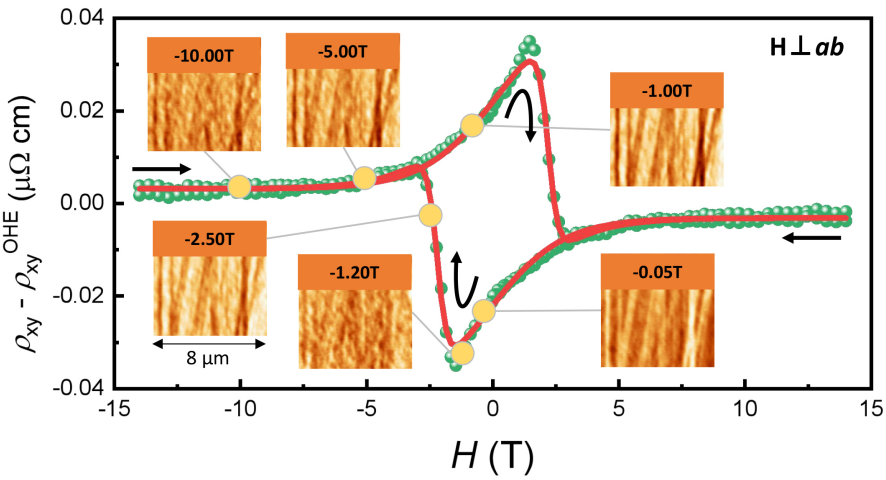

Figure 6. Hall resistivity and magnetic domain evolution under vertical magnetic fields. Field-dependent Hall resistivity (after subtracting the ordinary Hall contribution, ρ_{xy} - ρ_{xy}^{OHE}) measured at 25 K with the magnetic field applied perpendicular to the film plane (H ⊥ *ab*). Green symbols represent experimental data, while the thick red curve shows the fit using a two-channel AHE model. The arrows indicate the magnetic field sweep direction. MFM images acquired at representative magnetic fields (-10.00 T, -5.00 T, -2.50 T, -1.20 T, -1.00 T, and -0.05 T) are overlaid, with yellow circles marking the corresponding positions on the Hall curve. OHE: ordinary Hall effect; AHE: anomalous Hall effect; MFM: magnetic force microscopy.

The MFM images reveal an anticorrelation between stripe-domain visibility and the Hall resistivity anomaly: stripe-like domains are pronounced at low fields (-0.05 T, -1.0 T) and high fields (> -5 T), but become significantly suppressed near -1.2 T - precisely where the Hall resistivity exhibits its peak feature. This anticorrelation suggests that the Hall anomaly may include contribution from spin-reorientation-induced transport anisotropy, possibly reflected by the peak structure: near -1.2 T, the competing interfacial and bulk anisotropies drive a transition from the noncollinear, stripe-domain state toward a more uniformly canted spin configuration, producing enhanced spin-chirality-dependent scattering that is not captured by the two-channel AHE model.

The two-channel AHE model assumes isotropic magnetic properties and thus provides no information about the detailed spin configuration in our samples. The systematic underfitting of peak and valley regions may indicate residual contributions from the proposed noncollinear spin texture, which could reflect complex interplay between spin-orbit coupling and vertically varying spin reorientation in our superlattices. The observed anticorrelation between stripe-domain evolution and Hall resistivity anomaly is suggestive of a topological contribution, though we cannot fully exclude inhomogeneous magnetization dynamics or domain-reconfiguration effects as alternative origins. Our combined MFM, MAR measurements and micromagnetic simulations thus provide critical constraints on the spin configuration, revealing how interfacial engineering can stabilize novel magnetic textures that suppress topological skyrmions while generating distinctive magneto-transport signatures through noncollinear spin arrangements. Although our observational results cannot quantitatively determine the relative energy scales of interfacial exchange interaction and DMI, the idea that interfacial exchange competes with or inhibits DMI is still a physically reasonable assumption that is consistent with the observed magnetic microstructure. Future work that combines element-specific spectroscopic analysis with first-principles calculations might be able to obtain the microscopic parameters needed to directly verify this assumption.

Thickness-dependent transport properties

To assess the generality of our observations, we systematically compared the transport properties across the three superlattice structures: L_9S_6, L_7S_6, and L_5S_5. As shown in Supplementary Figures 13-16, all three samples exhibit qualitatively similar Hall resistivity anomalies and temperature-dependent resistivity and magnetization behavior, indicating that the observed magnetic phenomena are robust features of the LCO/SRO superlattice architecture. Notably, the two-channel AHE model fits reveal that the interfacial L-loop component exhibits prominent dependence on LCO layer thickness [Supplementary Figure 13]. The temperature-dependent resistivity shows a slope change at approximately 75 ~ 85 K for all samples [Supplementary Figure 15A and B], which we attribute to the Curie temperature of the LCO layers. The negative magneto-resistivity increases with decreasing temperature for all samples except peaked at respective critical temperatures as labeled by arrows with different colors [Supplementary Figure 15C]. The field-dependence of the magneto-resistivity is more significant for L_5S_5 [Supplementary Figure 15D], suggesting that the thickness of LCO layers has a complex correlation to the spin-dependent scattering. These thickness-dependent trends support our interpretation that the observed anisotropic stripe pinning and multi-fold MAR symmetry originate from interfacial exchange coupling. While these thickness-dependent trends are consistent with the proposed interfacial coupling picture, a more comprehensive study with additional samples - particularly structures with sub-unit-cell SRO thicknesses and variable LCO/SRO periodicities - would be needed to fully establish the quantitative relationship between layer thickness, strain state, and magnetic properties, and to rule out alternative explanations such as disorder-induced localization effects.

CONCLUSIONS

We synthesized LCO/SRO superlattices on STO substrates with various combinations of layer thicknesses using PLD. One-dimensional magnetic stripe-like domains are induced by out-of-plane magnetic field at intermediate strengths (~ 1 T) rather than in-plane field, indicating a strong magnetic anisotropic pinning in these superlattice samples. Field- and temperature-dependent magneto-transport measurements show that these stripe-like domains are associated with elimination of conductivity and exhibits complex combinations of rotation-symmetric components that evolve systematically with experimental conditions. We propose a model of vertically varying noncollinear spin configuration within the SRO layers, where spins reorient from out-of-plane in the bulk interior to in-plane near the interfaces due to strong exchange coupling with LCO. This proposed spin texture provides a consistent explanation for the observed MAR results and micromagnetic simulation results. No skyrmion structures are observed even at 10 T, suggesting that interfacial exchange interaction along with DMI may be insufficient for the appearance of skyrmionic features. Instead, stripe-like domains are stabilized in these superlattice samples. Our results demonstrate that superlattice design can influence emergent magnetic effects, including magneto-transport anomalies and magnetic anisotropy, providing experimental guidance for potential spintronic applications.

DECLARATIONS

Acknowledgement

We thank the staff members of the SMA System (https://cstr.cn/31125.02.SHMFF.SM2.SMA) at the Steady High Magnetic Field Facility, CAS (https://cstr.cn/31125.02.SHMFF), for providing technical support and assistance in data collection and analysis.

Authors' contributions

Experimental design: Huang, H.; Lu, Y.
Experiments and data collection: Jiang, Z.; Zhao, K.; Meng, W.; Hou, Y.; Cui, Z.; Zhang, J.; Shan, Z.; Lu, Q.
Theoretical modelling and simulations: Zhang, Z.; Zhao, Y.
Data analysis: Jiang, Z.; Zhao, K.; Meng, W.; Zhang, Z.; Zhao, Y.
Manuscript writing and revision: Zhang, Z.; Huang, H.; Lu, Y.
Supervision: Lu, Y.

Availability of data and materials

The data supporting the findings of this study are available within this Article and its Supplementary Materials. Further data are available from the corresponding authors upon request.

AI and AI-assisted tools statement

During the preparation of this manuscript, the AI tool Kimi (version K2.5, released 2026-01-27) was used solely for language editing. The tool did not influence the study design, data collection, analysis, interpretation, or the scientific content of the work. All authors take full responsibility for the accuracy, integrity, and final content of the manuscript.

Financial support and sponsorship

This work was supported by Guangdong Major Project of Basic Research (2025B0303000004), the Natural Science Foundation of Anhui Province (2208085ME113), Hefei National Lab (ZB2025020100), Guangdong Provincial Quantum Science Strategic Initiative (GDZX2501001, GDZX2401003 and GDZX2401004), National Key R&D Program of China (2023YFA1607701, 2024YFA1408101), National Natural Science Foundation of China (51627901 and 12527803) and the support from Station of Quantum Materials.

Conflicts of interest

All authors declared that there are no conflicts of interest.

Ethical approval and consent to participate

Not applicable.

Consent for publication

Not applicable.

Copyright

Supplementary Materials

Supplementary Materials

REFERENCES

1. Gong, L.; Jiang, H.; Lao, B.; et al. Intrinsic strain-driven topological evolution in $SrRuO_3$ via flexural strain engineering. *Adv. Elect. Mater*. **2025**, *11*, e00364. DOI
2. Wakabayashi, Y. K.; Kobayashi, M.; Seki, Y.; et al. $SrRuO_3$ under tensile strain: Thickness-dependent electronic and magnetic properties. *J. Appl. Phys.* **2024**, *136*, 043907. DOI
3. Zhang, S.; Mu, X.; Yang, Q.; et al. Atomic structure of the phase interface in hafnium oxide-based thin films. *Microstructures* **2025**, *5*, 2025069. DOI
4. Liu, J.; Zhu, H.; Liu, F.; et al. Defect-induced interfacial modulation for enhanced resistive switching performance in antiferroelectric/ferroelectric heterostructures. *Microstructures* **2025**, *5*, 2025064. DOI
5. Chen, Z.; Liu, Y.; Zhang, H.; et al. Electric field control of superconductivity at the $LaAlO_3/KTaO_3(111)$ interface. *Science* **2021**, *372*, 721-4. DOI
6. Ding, Z.; Chen, X.; Liao, L.; et al. From ferromagnet to antiferromagnet: dimensional crossover in (111) $SrRuO_3$ ultrathin films. *Chin. Phys. Lett.* **2025**, *42*, 120709. DOI
7. Gozar, A.; Logvenov, G.; Kourkoutis, L. F.; et al. High-temperature interface superconductivity between metallic and insulating copper oxides. *Nature* **2008**, *455*, 782-5. DOI
8. Reyren, N.; Thiel, S.; Caviglia, A. D.; et al. Superconducting interfaces between insulating oxides. *Science* **2007**, *317*, 1196-9. DOI
9. Hwang, H. Y.; Iwasa, Y.; Kawasaki, M.; Keimer, B.; Nagaosa, N.; Tokura, Y. Emergent phenomena at oxide interfaces. *Nat. Mater.* **2012**, *11*, 103-13. DOI
10. Fert, A.; Reyren, N.; Cros, V. Magnetic skyrmions: advances in physics and potential applications. *Nat. Rev. Mater.* **2017**, *2*, 17031. DOI
11. Zhang, H.; Ma, Y.; Zhang, H.; et al. Thermal spin injection and inverse edelstein effect of the two-dimensional electron gas at EuO-$KTaO_3$ interfaces. *Nano. Lett.* **2019**, *19*, 1605-12. DOI
12. Peng, S.; Zheng, X.; Li, S.; et al. Unconventional scaling of the orbital Hall effect. *Nat. Mater.* **2025**, *24*, 1749-55. DOI
13. Guo, Y.; Chen, A.; Zeng, Z.; et al. Magnetic memory driven by spin splitting torque in nonrelativistic collinear antiferromagnet. *Nat. Commun.* **2025**, *17*, 1309. DOI PubMed PMC

14. Rambabu, A.; Sundaresan, A. Magnetic and electrical properties of $LaCoO_3$ - $LaNiO_3$ epitaxial thin films on $LaAlO_3$ substrate. *Mater. Today:. Proc.* **2023**, S2214785323008192. DOI
15. Aso, R.; Kan, D.; Shimakawa, Y.; Kurata, H. Control of structural distortions in transition-metal oxide films through oxygen displacement at the heterointerface. *Adv. Funct. Mater.* **2014**, *24*, 5177-84. DOI
16. Meng, K.; Ahmed, A. S.; Baćani, M.; et al. Observation of nanoscale skyrmions in $SrIrO_3$/$SrRuO_3$ bilayers. *Nano. Lett.* **2019**, *19*, 3169-75. DOI
17. Mühlbauer, S.; Binz, B.; Jonietz, F.; et al. Skyrmion lattice in a chiral magnet. *Science* **2009**, *323*, 915-9. DOI
18. Huang, Z.; Wang, Z.; Li, B.; et al. Angular-dependent topological Hall effect in $Tm_3Fe_5O_{12}$ on $SrRuO_3$. *Adv. Funct. Mater.* **2026**, *36*, e13700. DOI
19. Yang, M.; Li, Q.; Chopdekar, R. V.; et al. Creation of skyrmions in van der Waals ferromagnet Fe_3GeTe_2 on $(Co/Pd)_n$ superlattice. *Sci. Adv.* **2020**, *6*, eabb5157. DOI
20. Singh, S.; Basha, M. A.; Prajapat, C. L.; et al. Antisymmetric magnetoresistance and helical magnetic structure in a compensated Gd/Co multilayer. *Phys. Rev. B.* **2019**, *100*, 140405. DOI
21. Cai, Y.; Deng, X.; Hu, C.; et al. Robust strain in freestanding single-crystal $SrRuO_3$ membranes. *ACS. Appl. Nano. Mater.* **2024**, *7*, 10670-8. DOI
22. Gu, Y.; Wang, Q.; Hu, W.; et al. An overview of $SrRuO_3$-based heterostructures for spintronic and topological phenomena. *J. Phys. D:. Appl. Phys.* **2022**, *55*, 233001. DOI
23. Magnus, F.; Arnalds, U. B.; Palonen, H.; et al. Tuneable exchange-spring stiffness in amorphous magnetic trilayer structures. *J. Phys:. Condens. Matter.* **2021**, *33*, 445803. DOI
24. Soumyanarayanan, A.; Raju, M.; Gonzalez Oyarce, A. L.; et al. Tunable room-temperature magnetic skyrmions in Ir/Fe/Co/Pt multilayers. *Nat. Mater.* **2017**, *16*, 898-904. DOI
25. Lisfi, A.; Lodder, J. C. Magnetic domains in epitaxial $BaFe_{12}O_{19}$ thin films with perpendicular anisotropy. *J. Phys.:. Condens. Matter.* **2002**, *14*, 12339. DOI
26. De'Bell, K.; Macisaac, A. B.; Whitehead, J. P. Dipolar effects in magnetic thin films and quasi-two-dimensional systems. *Rev. Mod. Phys.* **2000**, *72*, 225-57. DOI
27. Nagaosa, N.; Sinova, J.; Onoda, S.; Macdonald, A. H.; Ong, N. P. Anomalous Hall effect. *Rev. Mod. Phys.* **2010**, *82*, 1539-92. DOI
28. Verma, N.; Addison, Z.; Randeria, M. Unified theory of the anomalous and topological Hall effects with phase-space Berry curvatures. *Sci. Adv.* **2022**, *8*, eabq2765. DOI PubMed PMC
29. Chen, Z.; Xu, X.; Qiu, X.; et al. Manipulation of magnetism and Hall effects in oxide superlattices by dimensionality crossover and interfacial Dzyaloshinskii-Moriya interaction. *Adv. Funct. Mater.* **2026**, *36*, e24217. DOI
30. Niu, X.; Chen, B.; Zhong, N.; Xiang, P.; Duan, C. Topological Hall effect in $SrRuO_3$ thin films and heterostructures. *J. Phys:. Condens. Matter.* **2022**, *34*, 244001. DOI
31. Wang, W.; Daniels, M. W.; Liao, Z.; et al. Spin chirality fluctuation in two-dimensional ferromagnets with perpendicular magnetic anisotropy. *Nat. Mater.* **2019**, *18*, 1054-9. DOI
32. Matsuno, J.; Ogawa, N.; Yasuda, K.; et al. Interface-driven topological Hall effect in $SrRuO_3$-$SrIrO_3$bilayer. *Sci. Adv.* **2016**, *2*, e1600304. DOI
33. Kim, G.; Son, K.; Suyolcu, Y. E.; et al. Inhomogeneous ferromagnetism mimics signatures of the topological Hall effect in$SrRuO_3$ films. *Phys. Rev. Mater.* **2020**, *4*, 104410. DOI
34. Cuoco, M.; Di Bernardo, A. Materials challenges for $SrRuO_3$: from conventional to quantum electronics. *APL. Materials.* **2022**, *10*, 090902. DOI
35. Tang, J.; Xu, G.; You, Y.; et al. Abnormal peak of angular-dependent Hall effect as an indicator for skyrmion in perpendicular magnetic anisotropy system. *Appl. Phys. Lett.* **2020**, *117*, 202402. DOI
36. Tian, D.; Liu, Z.; Shen, S.; et al. Manipulating Berry curvature of $SrRuO_3$ thin films via epitaxial strain. *Proc. Natl. Acad. Sci. U.S.A.* **2021**, *118*, e2101946118. DOI
37. Mehta, V. V.; Biskup, N.; Jenkins, C.; Arenholz, E.; Varela, M.; Suzuki, Y. Long-range ferromagnetic order in $LaCoO_{3-\delta}$ epitaxial films due to the interplay of epitaxial strain and oxygen vacancy ordering. *Phys. Rev. B.* **2015**, *91*, 144418. DOI
38. Zahradník, M.; Uhlířová, K.; Maroutian, T.; et al. Magnetic domain wall motion in $SrRuO_3$ thin films. *Materials. &. Design.* **2020**, *187*, 108390. DOI
39. Wang, W.; Li, L.; Liu, J.; et al. Magnetic domain engineering in $SrRuO_3$ thin films. *npj. Quantum. Mater.* **2020**, *5*, 73. DOI
40. Grutter, A. J.; Wong, F. J.; Arenholz, E.; Vailionis, A.; Suzuki, Y. Evidence of high-spin Ru and universal magnetic anisotropy in $SrRuO_3$ thin films. *Phys. Rev. B.* **2012**, *85*, 134429. DOI

41. Sahoo, J.; Vagadia, M.; Hübner, R.; et al. Role of competing magnetic anisotropies in deriving topologically nontrivial spin textures in oxide heterostructures. *Phys. Rev. B.* **2024**, *110*, 104422. DOI
42. Zhou, L.; Tanwani, M.; Tong, P.; et al. Harness of room-temperature polar skyrmion bag in oxide superlattice. *Nat. Commun.* **2025**, *16*, 9911. DOI PubMed PMC
43. Yu, X. Z.; Onose, Y.; Kanazawa, N.; et al. Real-space observation of a two-dimensional skyrmion crystal. *Nature* **2010**, *465*, 901-4. DOI
44. Buhrandt, S.; Fritz, L. Skyrmion lattice phase in three-dimensional chiral magnets from Monte Carlo simulations. *Phys. Rev. B.* **2013**, *88*, 195137. DOI
45. Prasetiyawati, R. D.; Song, S.; Kwon, S.; et al. Engineering hall resistivity anomalies in epitaxial $SrRuO_3$ thin films by Mo doping. *ACS. Appl. Mater. Interfaces.* **2025**, *17*, 63540-8. DOI